Stochastic-Deterministic Population Balance Modeling and Simulation of a Fluidized Bed Crystallizer Experiment

Clemens Bartsch[a,1], Viktoria Wiedmeyer[b,1], Zahra Lakdawala[a], Robert I.A. Patterson[a], Andreas Voigt[c], Kai Sundmacher[c,d], Volker John[a,e,*]

[a] *Weierstrass Institute for Applied Analysis and Stochastics (WIAS), Mohrenstr. 39, 10117 Berlin, Germany*

[b] *ETH Zurich, Institute of Process Engineering, Sonneggstrasse 3, 8092 Zurich, Switzerland*

[c] *Otto-von-Guericke-University Magdeburg, Department Process Systems Engineering, Universitätsplatz 2, 39106 Magdeburg, Germany*

[d] *Max Planck Institute for Dynamics of Complex Technical Systems, Process Systems Engineering, Sandtorstr. 1, 39106 Magdeburg, Germany*

[e] *Freie Universität Berlin, Department of Mathematics and Computer Science, Arnimallee 6, 14195 Berlin, Germany*

Abstract

The crystallization of potassium aluminum sulfate dodecahydrate (potash alum) in a fluidized bed crystallizer is studied both with experiments and simulations. A population balance system with three spatial coordinates and one internal coordinate (mass) is utilized as our model. The simulations are performed with a stochastic-deterministic method with novel extensions, where the fluid dynamics of the crystallizer (flow field, temperature, concentration) are solved deterministically and the particles are simulated with a stochastic method. In experiments of 30 min duration, the average crystal diameter increases by growth and agglomeration from about 130 μm to 210 μm. This observation agrees qualitatively well with our simulation results. A quantitative difference between simulation and experiment leaves room for future improvements in modeling.

*Corresponding author

Email addresses: bartsch@wias-berlin.de (Clemens Bartsch), wiedmeyv@ipe.mavt.ethz.ch (Viktoria Wiedmeyer), lakdawala@wias-berlin.de (Zahra Lakdawala), patterson@wias-berlin.de (Robert I.A. Patterson), andreas.voigt@ovgu.de (Andreas Voigt), sundmacher@mpi-magdeburg.mpg.de (Kai Sundmacher), john@wias-berlin.de (Volker John)

[1] Contributed equally to this work: Clemens Bartsch and Viktoria Wiedmeyer

Keywords: Fluidized bed crystallizer; Potassium aluminum sulfate dodecahydrate; Agglomeration; Population balance system; Stochastic-deterministic simulation method; Size separation

1. Introduction

A fluidized bed crystallizer (FBC), also called Oslo crystallizer, is a typical industrial crystallization device (Beckmann, 2013; Tavare, 1995) used in the pharmaceutical industry, particularly to grow crystal fractions into larger sizes of uniform size distribution (Beckmann, 2013; Lewis et al., 2015). In crystallization devices, a crystal size increase is typically achieved by two main mechanisms: growth and agglomeration. Both phenomena occur simultaneously at a certain minimal supersaturation. During agglomeration, supersaturation results in the formation of bridges between primary crystals. Agglomerates have a greater surface, higher porosity, smaller mass, and less regular shapes than primary crystals of a similar size. The main process parameters affecting the intensity of agglomeration inside the FBC are the temperature, the fluid composition, and the fluid velocity. Particles with relative particle velocities may collide in various angles. The relative particle velocity can be caused by non-aligned trajectories, inertia for particles of different sizes, and velocity gradients. A certain percentage of these collisions is 'effective' in the sense that an agglomerate forms.

Agglomeration was experimentally observed in a fluidized bed for potassium containing compounds (Lin et al., 2003). In the fluidized bed of Seckler et al. (1996) growth occurs, but agglomeration is the process of interest for phosphate removal in a fluidized bed during precipitation. The particle motion in a fluidized bed was investigated by simulations (Garcia-Gutierrez et al., 2017). In the FBC setup of Binev (2015), segregation occurs as a result of a model including gravitation and drag. In their experiments, large crystals and agglomerates are removed from the system and hence, growth is modeled but agglomeration is not. Binev (2015) and Hoffmann et al. (1993) demonstrate that particles of large diameter segregate to lower regions of an FBC while smaller ones segregate upward. According to Nienow and Naimer (1980), Binev (2015)and Zhang et al. (2009) argue that sedimentation is determined by the flow regime. According to Binev (2015), it is mentioned by Howley and Glasser (2002) that a prediction for the segregation and the particle size distributions in fluidized beds is not yet available. Kerst et al. (2017) started to close this gap by applying a CFD-DEM approach to simulate an FBC for a short time period. They observed that vertical relative velocities increase with particle size.

In the present work, the FBC is used for the crystallization of potash alum ($KAl(SO_4)_2 \cdot 12H_2O$). Potash alum has some industrial use nowadays, for example, it is used as an astringent in deodorants or in alum blocks applied on

the skin after shaving. For experiments and simulations, it is used as a model substance for crystallization since it is inexpensive to purchase, innocuous, soluble in water, it agglomerates easily, and many of its material properties and its solution kinetics are well known. In particular, it forms regular octahedral crystals.

The primary goal of the FBC is to obtain particles of a particular size. A derived goal is to have a height separation of different crystal fractions, i.e., to 'harvest' crystal fractions of a certain size from different heights in the FBC vessel. In this paper, a crystallization device of this kind is studied using experiments as well as numerical simulations that are based on the model of a population balance system. The models and numerical algorithms presented by Bartsch et al. (2019) for a tube crystallizer are extended to an FBC. The numerical approach employs a deterministic way of solving the system of equations for flow, temperature, and concentration. A stochastic method is utilized for solving the population balance equation for the crystals. The models and numerical methods from Bartsch et al. (2019) have been extended considerably: a turbulence model had to be included for the flow, collisions of particles with walls had to be taken into account, and a model for the sedimentation of particles had to be incorporated. These extensions are presented below in detail. Comparisons of experimental and numerical results show good qualitative and reasonable quantitative agreement.

This paper is organized as follows. First, in Section 2, the experimental setup, crystallization procedures, and operation conditions are introduced. Section 3 provides the population balance system to model the considered process. For each equation of this model, the numerical methods used to solve the system of equations are briefly described in Section 4. In Section 5, the numerical results are presented and comparisons with experimental results are performed. The paper concludes with an outlook in Section 6.

2. The Experiments

In this section, an example FBC developed in the group 'Lehrstuhl für Systemverfahrenstechnik' at OVGU Magdeburg is introduced. It was used for a series of experiments, details are provided and are the subject of the numerical work in later sections.

2.1. Design Setup of the Fluidized Bed Crystallizer

The FBC is shown photographically and diagrammatically in Figure 1. The central unit of the device is an upside-down bottle of 0.5 m height. The vessel is part of a closed circuit of a streaming suspension that contains the suspension

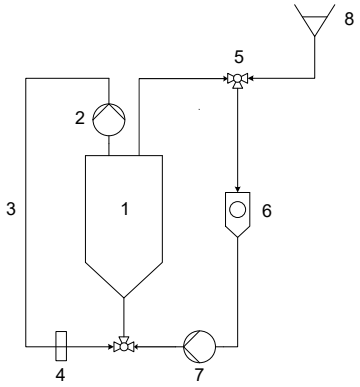

Figure 1: Left: The investigated example fluidized bed crystallizer (FBC); Right: Schematic of the FBC and its peripheral flow equipment: 1 FBC, 2 gear pump, 3 main flow circuit, 4 degasifier, 5 three-way valve, 6 flow-through microscope, 7 peristaltic pump, 8 seed addition funnel.

necessary to excite the desired crystal growth mechanisms. The crystallization vessel and the tube periphery are surrounded by a cooling jacket for temperature control. The flow enters the bottom of the vessel (1 in the diagram in Figure 1.) and exits through a filter at the top, entering the main flow circuit (3) equipped with a pump (2) and a degasifier (4). Afterwards, the fluid re-enters the FBC from below and keeps the crystals in the FBC fluidized. The crystals remain in the main vessel and do not enter the exterior main flow circuit. The pump (2) is additionally protected from crystals by a filter for operation outside of the regime described in this work.

The other external cycle serves as sampling loop for inline imaging of the suspension. A withdrawal tube can be positioned at variable heights in the vessel. The withdrawn suspension is pumped (7) through a flow-through cell (Lixell, Sympatec) of a video microscope (Qicpic, Sympatec) (6). One minute of a recorded binary video corresponds to 120 frames as shown in Figure 2. The crystal size and shape distribution of the imaged crystal population is determined. The crystal projections in each frame are evaluated using shape estimation algorithms (Borchert et al., 2014). Projected objects are classified as agglomerates when their solidity is less than 0.9. The solidity measures the objects' concavity and equals 1 for a convex object. The degree of agglomeration is defined as the ratio of the number of agglomerates to the number of agglomerates plus primary particles. Primary particles with an eccentricity below 0.3, where a circle has zero eccentricity, are classified as bubbles and are discarded. For comparison with the simulation of spherical particles, all experimental results are shown in terms of the sphere equivalent diameter of primary particles and agglomerates. The sphere equivalent diameter is calculated from the projected area.

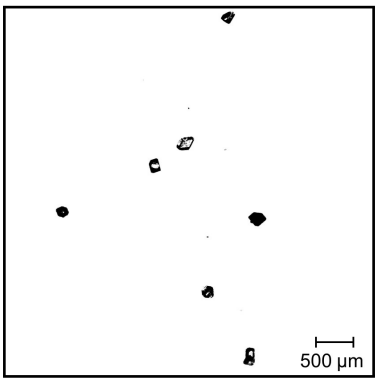

Figure 2: A snapshot of crystallizer suspension, containing primary and agglomerated potash alum crystals.

2.2. Operating Conditions, Experimental Procedures, and Parameters

During preparation of an experiment, potash alum ($KAl(SO_4)_2 \cdot 12H_2O$) seed crystals (Merck, CAS No. 7784-24-9, purity $\geq 99\,\%$) were sieved with meshes of 125 µm and 150 µm size. The crystallizer was filled with potash alum and purified water. The solution was heated to at least 23 °C to ensure that all crystals were dissolved. Following Temmel et al. (2016), the initial equilibrium saturation temperature of the solution was 17 °C to 18 °C. Prior to seed addition, the solution was cooled until the equilibrium supersaturation was 6 % to 8 %. Supersaturation is the main driving force for crystal growth and crystal agglomeration. An intermediate supersaturation is chosen where growth and agglomeration rates are relatively small. Before a significant crystal size increase can be observed, long crystal residence times are necessary which implies long run times.

The FBC volume is 5 l and the periphery volume is about 0.5 l. At positions 2 and 7 in Figure 1 (right), the mass flow was set to 55 kg/h for the main flow circuit and 53 kg/h for the sampling and seeding circuit.

The mass of seed crystals was 1×10^{-4} kg in all experiments. An additional preliminary experiment was carried out for twice this seed mass, i.e., 2×10^{-4} kg, but no qualitative change was observed and the seed mass was not further of interest. For the chosen seed mass of 1×10^{-4} kg, the resulting initial suspension density was $0.02\,\mathrm{kg\,m^{-3}}$. Two different methods of seed addition were applied to analyze the importance of the seeding position for the simulations. In the first method labeled 'top seeding', seed crystals were added from the top of the FBC. In the second method labeled 'bottom seeding', seed crystals were added through the funnel at position 8 in Figure 1 right and, hence, through the flow-through cell and entered the FBC from the bottom.

A total of 12 experiments (labeled A to L) with varying seeding strategies and withdrawal heights were conducted. Details are given in Table 1, and in Figure 3.

experiment name	seed addition position	height
A	top	$z = 0\,\mathrm{m}$
B	top	$z = 0\,\mathrm{m}$
C	bottom	$z = 0\,\mathrm{m}$
D	top	$z = 0.1\,\mathrm{m}$
E	top	$z = 0.1\,\mathrm{m}$
F	bottom	$z = 0.1\,\mathrm{m}$
G	bottom	$z = 0.1\,\mathrm{m}$
H	bottom	$z = 0.1\,\mathrm{m}$
I	top	$z = 0.30\,\mathrm{m}$
J	top	$z = 0.17\,\mathrm{m}$
K	top	$z = 0.17\,\mathrm{m}$
L	bottom	$z = 0.17\,\mathrm{m}$

Table 1: Overview of the experiments.

The sampling circuit can withdraw suspension in an adjustable height measured from the FBC bottom in the range of $z = 0\,\mathrm{m}$ to $0.5\,\mathrm{m}$. In experiment I at $z = 0.3\,\mathrm{m}$, only a few crystals were observed. Thus, three lower withdrawal positions were selected. Their distance from the FBC bottom is $0\,\mathrm{m}$, $0.10\,\mathrm{m}$ and $0.17\,\mathrm{m}$. When the crystals observed in experiment I are included in the averaged results for the highest withdrawal position, the position is marked with an asterisk as $0.17\,\mathrm{m}^*$.

All experimental results were averaged over the same type of experiment regarding seeding strategy and withdrawal height. For averaging, the variables of interest, e.g., the mean diameter, was not calculated for each experiment separately and averaged afterwards but the diameter of the crystals of all experiments were averaged. Similar absolute crystal numbers were observed in experiments of the same type. Thus, a weighting of the experiments was not considered necessary. The absolute crystal numbers are shown in Figure 3 at the average time point of all videos. Not in all experiments, a video was taken at each time point. The videos had a duration of $30\,\mathrm{s}$ to $201\,\mathrm{s}$ at a frame rate from 10 frames per second to 20 frames per second. In Figure 3, the crystal number is normed to 2400 frames as for a typical video of $120\,\mathrm{s}$ length and 20 frames.

2.3. Observable Experimental Phenomena

In all experiments, a high number of nuclei was observed. The nuclei showed a slight increase in the degree of agglomeration but not in the mean equivalent sphere diameter. The nuclei remained in the size range below $50\,\mu\mathrm{m}$ during the whole experiment and were thus easy to distinguish from the seed fraction that was of interest in the simulations. Although the nuclei appear in a high number, their total mass always remained below 3 % of the mass of all observed crystals. It is assumed that the nuclei are not influencing the supersaturation and, hence,

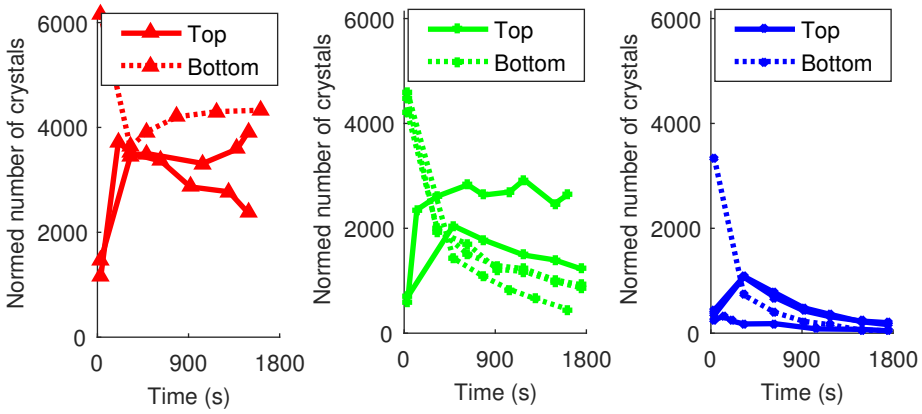

Figure 3: Absolute crystal number normed to 2400 frames of each experiment. Experiments at different heights $z = 0\,\mathrm{m}$ (left), $z = 0.1\,\mathrm{m}$ (middle), and $z = 0.17\,\mathrm{m}^*$ (right). Legend shows seeding type.

the desired seed fraction. Therefore, all observed crystals which are smaller than 50 µm were neglected in Figure 3 and they are neglected in the following for the calculation of the average diameter and of the degree of agglomeration.

In Figure 3, the absolute number of crystals decreases strongly after the first video for bottom seeding since initially all seed crystals pass the cuvette. Already in the second video, the crystal number is very similar for both seeding types. During the experiment, at the highest position in the FBC, the absolute number of crystals is very small. After seeding, the crystal number decreases at the highest and at the intermediate position for all except one experiment. No clear trend can be observed at the bottom position. A decreasing total crystal number at increasing crystal size may result from agglomeration. Overall, most crystals accumulate at the bottom of the FBC.

The optical density was analyzed for each image. It is in average below the maximum optical density recommended by the manufacturer for all experiments and videos but in the first video of some experiments. In this case, the number of crystals overlapping in an image increases which leads to a higher probability of primary particles classified wrongly as agglomerates. This slightly raises the degree of agglomeration in the first video compared to its actual value. The degree of agglomeration was defined in Section 2.1. It measures the proportion of agglomerates in the vessel. Simultaneously considering the degree of agglomeration and the total crystal number allows to estimate the extent of the different crystallization phenomena. If agglomeration occurs in the process, the degree of agglomeration increases over time while the crystal number reduces. Breakage may decrease the degree of agglomeration and raises the crystal number. Figure 4 shows that the average degree of agglomeration is between 9 % and 47 %.

High degrees of agglomeration are observed in the first and partly still in the second video. For bottom seeding this may be caused by loose agglomeration or overlapping crystal projections in an image at high suspension densities. For top seeding this may be caused by a faster sinking of large agglomerates. At all heights, the degree of agglomeration decreases right after the start. In the later time of the experiment after around 900 s, the portion of agglomerates increases slightly at the bottom position. At the lowest position, the degree of agglomeration of top and bottom seeding is similar. For the other heights, the degrees of agglomeration for top are lower than for bottom seeding. Most crystals are located at the bottom and, hence, the average degree of agglomeration of all crystals in the FBC is similar for top and bottom seeding. The seeding type has no or little impact on size distributions of the crystals. The distribution was slightly shifted to smaller sizes for bottom seeding experiments but qualitatively the same increase in size was observed over time. Hence, the two seeding methods are not considered separately in this work but the results are averaged over both methods. In the following sections of this work, all observed crystals are analyzed, i.e., the primary crystals and agglomerates are not further distinguished but cumulated.

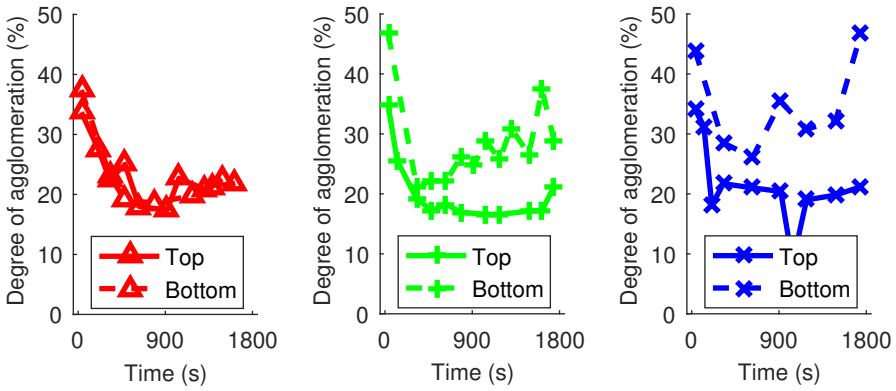

Figure 4: Degree of agglomeration of crystals at different heights $z = 0\,\mathrm{m}$ (left), $z = 0.1\,\mathrm{m}$ (middle), and $z = 0.17\,\mathrm{m}^*$ (right) for top (solid line) and bottom (dashed line) seeding. Experiments of the same seeding time and height were averaged for videos of identical frame rate.

In the following, the findings which are relevant to the simulation setup are summarized. At the start, the seed addition position influences which crystals can be seen in which height. During the experiment, the results are independent of the seeding position. Hence, for the simulations, the location of the seed addition can be freely chosen but should be kept in mind for comparison. Nucleation affects the supersaturation just to a very small extent. The nuclei remain at small sizes and can be separated from the seed fraction by image post-processing. Therefore, nuclei are neglected in the simulation. Most crystals are located at the lowest position. Furthermore, there is a considerable portion of

agglomerates in the crystallizer. The degree of agglomeration increases only slightly during the experiments. Hence, agglomeration should be considered in the simulations.

3. The Mathematical Model

Here, the multi-physics model included in the simulation framework for the FBC described in Section 2 is presented. The equations are defined on a spatial domain for a time interval, starting from 0 s up to some end time t_{end}, which depends on the experimental setup. For the FBC, the spatial coordinate space is a 3d bounded Lipschitz domain denoted by $\Omega_{\boldsymbol{x}}$. The inner coordinate space Ω_{m} is a 1d continuous property space using particle mass as coordinate. The flow field in the FBC is governed by the Navier–Stokes equations. For the numerical simulations, it has to be equipped with a turbulence model, see Section 3.1 for details. For brevity of presentation, the turbulence model is included in the (strong form of the) flow equations shown below although this model is actually mesh-dependent. The temperature and concentration fields are treated with convection-diffusion equations. Since these equations are convection-dominated, one needs for them a stabilized discretization. The used stabilization is the so-called FEM-FCT method, see Section 4.1. Since this method cannot be expressed by simply adding a single term, the convection-diffusion equations are given below without indicating the necessary numerical stabilization. The model equations are presented in the form of a population balance system consisting of flow, temperature, and concentration equations defined on $(0, t_{\text{end}}) \times \Omega_{\boldsymbol{x}}$ along with a population balance equation for the mass-based particle population density defined on $(0, t_{\text{end}}) \times \Omega_{\boldsymbol{x}} \times \Omega_{\text{m}}$:

$$\frac{\partial}{\partial t}\boldsymbol{u} - \nabla \cdot (\nu + \nu_{\text{Smago}} \|\nabla \boldsymbol{u}\|_F) \nabla \boldsymbol{u} + (\boldsymbol{u} \cdot \nabla)\, \boldsymbol{u} + \nabla \frac{p}{\rho} = \mathbf{g}, \tag{1a}$$

$$\nabla \cdot \boldsymbol{u} = 0,$$

$$\frac{\partial}{\partial t} T - D_T \Delta T + \boldsymbol{u} \cdot \nabla T = g_T I_{\text{growth}}(c, T, f), \tag{1b}$$

$$\frac{\partial}{\partial t} c - D_c \Delta c + \boldsymbol{u} \cdot \nabla c = g_c I_{\text{growth}}(c, T, f), \tag{1c}$$

$$\frac{\partial}{\partial t} f + \boldsymbol{u} \cdot \nabla f = \mathcal{C}(f) + \mathcal{G}(c, T, f). \tag{1d}$$

The velocity field is not influenced by the transported quantities and the particle size distribution (PSD), it is just one-way coupled into the system. Since there is only one internal coordinate to describe the particles, they are assumed to be of spherical form.

The most important variables, physical constants, and function expressions together with their associated units and values are listed in Table 2. All equations are equipped with suitable initial and boundary conditions. The boundary of the FBC consists of an inlet (bottom) Γ_{in}, outlet (top) Γ_{out}, and the wall(s) Γ_{wall}. In the following, the setup for each equation will be discussed in detail. For the numerical simulations, the population balance system was appropriately transformed to a non-dimensional form.

3.1. The Flow Field

The flow field is governed by the Navier–Stokes equations. Since the considered flows are turbulent, their numerical simulation requires the application of a turbulence model. This model is the nonlinear viscous term in (1a). The flow in the FBC is pumped with a mass flow rate between 50 and 200 $^{\text{kg}}/_{\text{h}}$, depending on the experimental setup. Assuming a parabolic inflow profile at the bottom inlet, the (mid-range value of) mass flow rate $\dot{m} = 93$ $^{\text{kg}}/_{\text{h}}$ translates into a characteristic average inflow velocity of $U \approx 0.08$ $^{\text{m}}/_{\text{s}}$. Together with the choice of a characteristic length $L = 0.1$ m as a typical inner diameter, the Reynolds number becomes $\text{Re} = \frac{\rho U L}{\mu} = 6000$. This number indicates that the flow is already mildly turbulent. A large eddy simulation (LES) model of Smagorinsky type is used to model the effects of unresolved flow scales. This model is a popular and simply to implement turbulence model, which effectively introduces an artificial, solution-dependent viscosity to the momentum balance equation (Smagorinsky, 1963), (John, 2016, Ch. 8), see the nonlinear contribution of the viscous term in (1a).

The fluid is initially considered to be at rest, i.e., $\boldsymbol{u} \equiv \boldsymbol{0}$ on $\Omega_{\boldsymbol{x}}$ at $t = 0$. A parabolic velocity profile is prescribed at the inflow (bottom) and outflow (top) of the crystallizer. Both inflow and outflow conditions are adapted to the mass flow rate, such that the flow is divergence-free. For example, for a mass flow rate of 93 $^{\text{kg}}/_{\text{h}}$, the average inflow and outflow velocity is calculated as $U_{\text{avg,in}} \approx 0.0783$ $^{\text{m}}/_{\text{s}}$ and $U_{\text{avg,out}} \approx 0.0014$ $^{\text{m}}/_{\text{s}}$. In order to avoid an impulsive start, both conditions are scaled by the time during the first second. The rest of the wall boundary is assigned the no-slip boundary condition $\boldsymbol{u} \equiv \boldsymbol{0}$.

3.2. The Temperature Field

The temperature field is governed by the convection-diffusion equation (1b). The source term on the right-hand side of (1b) models temperature sources due to crystallization, i.e., growth. It consists of a positive scaling parameter g_T and the growth intensity $I_{\text{growth}}(c, T, f)$, see Table 2.

The experiments were either run at constant temperature or by cooling down slightly and linearly over the course of an experiment. The tube and pump

Name	Notation	Units	Value/Function
Velocity	$\boldsymbol{u}$	m/s	
Pressure	p	Pa	
Temperature	T	K	
Molar concentration	c	$\mathrm{mol}/\mathrm{m}^3$	
Particle population density	f	$1/\mathrm{kg}\cdot\mathrm{m}^3$	
Spatial coordinate	$\boldsymbol{x}$	m	
Time	$\mathbf{t}$	s	
Gravity	$\mathbf{g}$	m/s^2	$(0, 0, -9.81)$
Fluid density	ρ	kg/m^3	1050
Dynamic viscosity	μ	$\mathrm{kg}/\mathrm{m}\cdot\mathrm{s}$	0.0014
Kinematic viscosity	ν	m^2/s	μ/ρ
Smagorinsky viscosity	ν_{Smago}	m^2/s	$C_{\mathrm{Smago}}\delta^2$
Filter width	δ	m	see Section 5.1
Smagorinsky coefficient	C_{Smago}	$-$	$5 \cdot 10^{-4}$
Frobenius norm of velocity gradient	$\|\nabla \boldsymbol{u}\|_F$	$1/\mathrm{s}$	
Diffusion coefficient (T)	D_T	m^2/s	$\frac{\lambda_{\mathrm{susp}}}{\rho_{\mathrm{susp}} C_{\mathrm{susp}}}$
Thermal conductivity	λ_{susp}	$\mathrm{W}/\mathrm{m}\cdot\mathrm{K}$	0.6
Suspension density	ρ_{susp}	kg/m^3	1050
Suspension specific heat capacity	C_{susp}	$\mathrm{J}/\mathrm{kg}\cdot\mathrm{K}$	3841
Scaling parameter (T)	g_T	$\mathrm{K}\cdot\mathrm{m}^3/\mathrm{kg}$	$\frac{\Delta h_{\mathrm{cryst}}}{\rho_{\mathrm{susp}} C_{\mathrm{susp}}}$
Crystallization enthalpy	$\Delta h_{\mathrm{cryst}}$	J/kg	89100
Diffusion coefficient (c)	D_c	m^2/s	$5.4 \cdot 10^{-10}$
Scaling parameter (c)	g_c	mol/kg	$-\frac{1}{M_{\mathrm{hydrate}}}$
Molar mass of hydrate	M_{hydrate}	kg/mol	0.4744
Agglomeration term	$\mathcal{C}(f)$	$1/\mathrm{kg}\cdot\mathrm{m}^3\cdot\mathrm{s}$	see Section 3.4
Growth term	$\mathcal{G}(c, T, f)$	$1/\mathrm{kg}\cdot\mathrm{m}^3\cdot\mathrm{s}$	see Section 3.4
Growth rate	$G(c, T, m)$	kg/s	see Section 3.4
Growth intensity	$I_{\mathrm{growth}}(c, T, f, t, \boldsymbol{x})$	$\mathrm{kg}/\mathrm{m}^3\cdot\mathrm{s}$	$\int_{\Omega_{\mathrm{m}}} G(c, T, m) f(t, \boldsymbol{x}, m)\ \mathrm{d}m$
Agglomeration scaling parameter	κ	$-$	see Section 3.4
Diameter of potash alum crystal	$d(m)$	m	$\sqrt[3]{6m/\rho_{\mathrm{cryst}}\pi}$
Mass of a potash alum crystal	m	kg	
Density of crystals	ρ_{cryst}	kg/m^3	1760
Boltzmann constant	k_B	J/K	$1.3806504 \cdot 10^{-23}$
Universal gas constant	R	$\mathrm{J}/\mathrm{K}\cdot\mathrm{mol}$	8.314

Table 2: Main notations and physical constants.

system were well isolated, a cooling hull surrounding the main crystallization vessel was used to control the temperature profile. Since the temperature profile varied very slowly over time, Dirichlet boundary conditions were applied everywhere. The Dirichlet value is a linear interpolation (in time) of the initial temperature and the final temperature.

Closely connected to the temperature is the solubility of the solvent in the solute, in our case potash alum in water. We used a fitted, fourth-order solubility model from Temmel et al. (2016). It is formulated in terms of mass potash alum dodecahydrate per mass added water, i.e., a type of mass loading. At temperature $\tilde{T}$ [°C], the hydrate-per-added-water mass loading in equilibrium is

$$w^{\mathrm{eq}}_{\mathrm{hyd},\mathrm{H_2O+}}(\tilde{T}) = a_1 + a_2\tilde{T} + a_3\tilde{T}^2 + a_4\tilde{T}^3 + a_5\tilde{T}^4 \quad \left[\frac{\text{kg hydrate}}{\text{kg added water}}\right], \quad (2)$$

with coefficients $a_1 = 0.0506$, $a_2 = 0.0023$, $a_3 = 7.76 \cdot 10^{-5}$, $a_4 = -2.43 \cdot 10^{-6}$, and $a_5 = 4.86 \cdot 10^{-8}$. This solubility model is assured to be valid in a temperature range between 10 °C and 60 °C, and therefore it is valid for the temperature at which the crystallizer was operated (around 15 °C). It enters the growth model in Section 3.4 via the supersaturation, since supersaturation is the driving force behind growth.

3.3. The Concentration Equation of the Dissolved Potash Alum

The concentration balance equation of dissolved aluminum potassium sulfate is described in (1c). The source term is the product of the growth intensity scaling parameter g_c and the growth intensity I_{growth} (see Table 2). Potassium alum is a (dodeca)hydrate, i.e., its crystal structure incorporates 12 water molecules per unit cell. If it is dissolved, the crystal structure is destroyed and the formerly bonded water molecules merge into the solvent water. Therefore, the dissolved substance is an *an*hydrate and not a hydrate anymore, a difference that will be encountered again when the growth model is discussed in Section 3.4. In the concentration equation, the loss of free water molecules due to bonding in the hydrate crystal structure is disregarded. This assumption follows from the primary assumption of constant density.

Homogeneous Neumann boundary conditions are applied at the wall and outflow of the FBC:

$$D_c \frac{\partial c}{\partial \mathbf{n}} = 0 \quad \text{on } \Gamma_{\mathrm{wall}} \cup \Gamma_{\mathrm{out}},$$

where $\mathbf{n}$ is the outward pointing unit normal vector. The Neumann condition implies that there is no change of concentration across the wall and outflow boundary. Cyclic Dirichlet boundary conditions are applied on the inlet Γ_{in}. The FBC is a closed system. However, the tubes, fittings, and pumps forming the closed circuit are disregarded except for the concentration balance. For the FBC, $t_{\mathrm{cyc}} = n\Delta t = 60\mathrm{s}$ is the time for the fluid to travel round the entire FBC circuit, where Δt is a constant time step and the n is the number of time steps required to complete a cycle. A list of inlet concentrations $c_{\mathrm{in},i} = (c_{\mathrm{in},0}, ..., c_{\mathrm{in},n-1})$, where $i = 0, ..., n-1$, is initialized for every cycle. Crystal growth reduces the amount of dissolved species and this amount is reflected in the inlet concentrations, see the detailed formulation in Bartsch (2018, Chapter 7). The starting value is derived from the experimental data and is described in detail by Borchert et al. (2014).

3.4. The Population Balance of the Potash Alum Crystals

The population balance equation for the mass-based particle population density has the form described in (1d). The collision-dominant agglomeration term has the form

$$\begin{aligned}\mathcal{C}(f,T,t,\boldsymbol{x},m) &= \frac{1}{2}\int_{\Omega_\mathrm{m}} K_{\mathrm{Brownian}}(T,m-\mu,\mu)f(t,\boldsymbol{x},m-\mu)f(t,\boldsymbol{x},\mu)\ \mathrm{d}\mu \\ &\quad - \int_{\Omega_\mathrm{m}} K_{\mathrm{Brownian}}(T,m,\mu)f(t,\boldsymbol{x},m)f(t,\boldsymbol{x},\mu)\ \mathrm{d}\mu.\end{aligned}$$

where m is the internal coordinate, i.e., agglomeration is modeled with an integral term as known from the Smoluchowski equation for agglomeration. The Brownian kernel reads as

$$K_{\mathrm{Brownian}}(T,m_1,m_2) = \kappa\frac{2Tk_B}{3\mu}\left(\frac{1}{d(m_1)}+\frac{1}{d(m_2)}\right)(d(m_1)+d(m_2)) \quad \left[\mathrm{m}^3/\mathrm{s}\right].$$

Choosing the kernel is always a delicate issue in modeling agglomeration processes. We decided to use the Brownian kernel here since it is well understood, we had good experience with it in other models, e.g., Anker et al. (2015), and finally, we obtained qualitatively correct results, see Section 5. The scaling parameter κ must, as usual, be fitted by means of numerical studies.

Given a fixed mass growth increment γ, [kg], the growth term is modeled by

$$\mathcal{G}(c,T,f,m) = \frac{G(c,T,m-\gamma)}{\gamma}f(m-\gamma) - \frac{G(C,T,m)}{\gamma}f(m),$$

a form that is well suited for stochastic particle simulation algorithms. In the considered temperature regime, relative supersaturation and thus the growth rate are relatively low, agglomeration dominates (both in terms of computational effort and in terms of effect on the system) in the simulations. For $G(.)$, an experimentally validated growth model from Temmel et al. (2016) is considered. It is based on a diameter-based one-dimensional Arrhenius-type model of the form

$$G_d = \frac{\sqrt{2}}{\pi^{\frac{1}{3}}}k_{\mathrm{G}_1}\exp\left(-\frac{k_{\mathrm{G}_2}}{RT}\right)\left(S_{\mathrm{hyd,H_2O+}}-1\right)^{k_{\mathrm{G}_3}} \quad \left[\mathrm{m}/\mathrm{s}\right]. \tag{3}$$

The model is used for a diameter-based 1d particle description with fitted parameters $k_{\mathrm{G}_1} = 5\cdot 10^7\ \mathrm{m}/\mathrm{s}$, $k_{\mathrm{G}_2} = 75\cdot 10^3\ \mathrm{J}/\mathrm{mol}$, $k_{\mathrm{G}_3} = 1.4$. The factor $\sqrt{2}/\pi^{\frac{1}{3}}$ is due to conversion from an octahedral to a spherical particle model. The growth rate G_d is only computed for $S_{\mathrm{hyd,H_2O+}} > 1$, otherwise, it is set to 0. The quantity $S_{\mathrm{hyd,H_2O+}}$ $[\mathrm{kg}/\mathrm{kg}]$ is the relative supersaturation of the solution. In the original reference, the mass of dissolved hydrate per added solvent (water) is used as a measure of the mass loading. In order to use it in the simulations, conversions have to be made. Let $w_{\mathrm{hyd,H_2O+}}$ $[\mathrm{kg}/\mathrm{kg}]$ be the current mass loading in that

measure and $w^{\mathrm{eq}}_{\mathrm{hyd,H_2O+}}(T)$ [kg/kg] be the mass loading in equilibrium, then the current supersaturation is

$$S_{\mathrm{hyd,H_2O+}} = \frac{w_{\mathrm{hyd,H_2O+}}}{w^{\mathrm{eq}}_{\mathrm{hyd,H_2O+}}(T)}. \tag{4}$$

While the equilibrium mass loading is given by the solubility curve (2), the current mass loading $w_{\mathrm{hyd,H_2O+}}$ must be gained by conversion from the molar concentration c, which is in units moles anhydrate per m^3 solution. First, one writes $w_{\mathrm{hyd,H_2O+}}$ as a function of the mass loading $w_{\mathrm{anhyd,H_2O}}$ [kg/kg] (mass anhydrate per total mass water):

$$w_{\mathrm{hyd,H_2O+}} = \frac{w_{\mathrm{anhyd,H_2O}}}{w_{\mathrm{anhyd,hyd}} - w_{\mathrm{anhyd,H_2O}}}. \tag{5}$$

Here, $w_{\mathrm{anhyd,hyd}} = {}^{M_{\mathrm{anhydrate}}}/_{M_{\mathrm{hydrate}}}$ is the constant mass fraction of anhydrate in the dodecahydrate crystal. Proceeding with

$$w_{\mathrm{anhyd,H_2O}} = \frac{c\, M_{\mathrm{anhydrate}}}{\rho}, \tag{6}$$

inserting (6) in (5), and the result in (4) gives a growth rate term in dependence on T and c, which is in accordance to our formulation of the model system. Finally, the diameter-based growth rate has to be converted into a mass-based growth rate, see Bartsch et al. (2019) for details.

A stochastic scheme is used to compute the agglomeration and growth term, which is described in detail in Bartsch (2018) and Bartsch et al. (2019).

4. Numerical Algorithms

This section starts with a brief description of the software and the discretizations used for performing the simulations. Then, those aspects of the numerical algorithms are explained in detail that are extensions in comparison to the algorithms used in Bartsch et al. (2019): the simulation of particle-wall collisions and of the sedimentation of particles.

4.1. Software and Discretizations

The in-house code ParMoon (Ganesan et al., 2016; Wilbrandt et al., 2017) is employed for the deterministic simulation of the flow field, the temperature, and the concentration. The population balance equation (1d) for the potash alum dodecahydrate crystals is solved with the stochastic particle simulation (SPS) in-house software Brush (Patterson et al., 2011). In theory, the model is mass based, whereas in ParMoon, the model is based on the number of hydrate

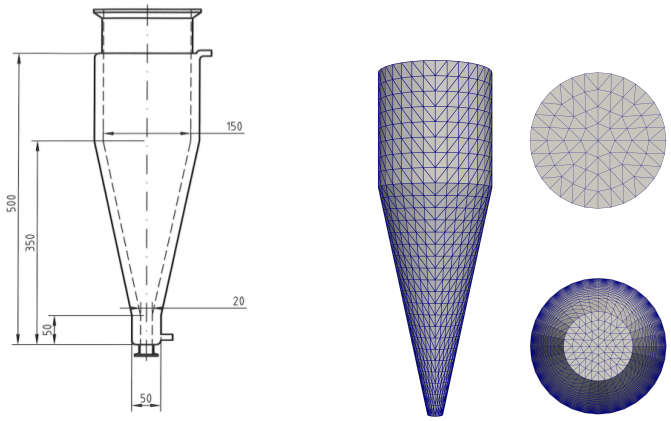

Figure 5: Geometry (in mm) and mesh used in the simulations. The inlet is cut off, the domain $\Omega_{\boldsymbol{x}}$ is regularly decomposed into 10752 tetrahedra of almost the same height, minimal diameter 15.0 mm, maximal diameter 38.9 mm. *Left:* Front view with measures in mm. *Right:* Top and bottom view.

molecules per particle. The conversion between both representations is done via Avogadro's constant N_A and the molar mass of potash alum dodecahydrate.

The technical configuration for the FBC is shown in Figure 5. The computational domain is simplified to take the form of a cylinder and a bottom-up truncated cone to represent the inner part of the crystallization vessel as shown in Figure 5 (right). It ignores the cylindrical pipe extensions/nozzles in the domain to enforce convexity of the domain, because the particle location algorithm from TETGEN relies on the assumption of convex domains. The spatial domain is then defined by

$$\begin{aligned}\Omega_{\boldsymbol{x}} \quad &= \quad \left\{(x,y,z) \in \mathbb{R}^3 : \sqrt{x^2+y^2} \leq 0.075, 0.3 \leq z \leq 0.45\right\} \\ &\quad \cup \left\{(x,y,z) \in \mathbb{R}^3 : \sqrt{x^2+y^2} \leq 0.01 + z \cdot \frac{0.065}{0.3}, 0 \leq z \leq 0.3\right\} \subset \mathbb{R}^3,\end{aligned}$$

where the lengths are given in m. In particular, the diameter of the inlet is 0.02 m.

For discretizing the flow equations (1a) in space, the popular Taylor–Hood pair of finite element spaces was utilized, i.e., the velocity is approximated by a continuous piecewise quadratic function and the pressure by a continuous piecewise linear function. On the grid depicted in Figure 5, one gets 51768 degrees of freedom (49419 for the velocity and 2349 for the pressure).

A Crank–Nicolson time discretization combined with a Picard iteration is applied to solve the flow equations (1a). A constant time step of $\Delta t = 0.05$ s turned

out to be suitable for performing stable simulations. As a solver for the linear problem in each step of the Picard iteration, a flexible GMRES method (Saad, 1993) preconditioned with the Least Squares Commutator Preconditioner with iterative solver (BiCGstab with SSOR preconditioner) for the velocity subproblem is used, see Ahmed et al. (2018) for a detailed description. This solver proved to be a good choice for time-dependent saddle point problems in Ahmed et al. (2018). The Picard iteration is forced to reduce the summed residual of momentum and continuity equation below $5 \cdot 10^{-9}$. This criterion was usually achieved after one or two iterations.

The temperature and concentration equations are discretized in time with the Crank–Nicholson approach and in space using P_1 finite elements on the tetrahedral discretization (2349 degrees of freedom for each equation). As stabilization, the linear FEM-FCT method (Kuzmin, 2009) is used, which has been proved to be a good compromise between accuracy and efficiency in John and Novo (2012); John and Schmeyer (2008) and which was used already within the simulation of other population balance systems, e.g., in Anker et al. (2015). This scheme is based on computing fluxes between the degrees of freedom of the finite element space and limiting them appropriately. It gives physically consistent results because it does not lead to spurious oscillations in the numerical solution. Since the resulting linear systems in every time step are relatively small, the sparse direct solver UMFPACK (Davis, 2004) is used for their solution.

In the SPS, particle transport and particle interaction are separated by a splitting scheme. Note that the SPS considers computational particles that approximate the particle population in each mesh cell, see Bartsch (2018); Bartsch et al. (2019) for details. A second order Strang splitting scheme, see Celnik et al. (2007), is used. The path of the computational particles is determined by the macroscopic velocity field, i.e., by the velocity field computed with the Smagorinsky LES model, and the sedimentation. To reduce the model complexity, we neglect the interaction of small particles with the unresolved scales in the flow; on this topic see e.g. Park et al. (2017). So-called 'turbulent diffusion' of physical particles would be captured numerically by adding appropriately weighted Gaussian noise to the particle trajectories simulated in the SPS.

In particular, a search routine for particle tracking is necessary, in order to determine the cell which contains a computational particle at a given time. The directed search algorithm from the in-house code TETGEN (Si, 2015) is utilized. In addition to determining the cell index, the algorithm also detects when a computational particle would leave the computational domain.

4.2. Particle-Wall Collisions

In the case that a computational particle hits a wall, it is important to distinguish the boundary through which the particle would leave. Particles leaving

through the inflow boundary are measured and removed from the simulation. In the case of wall or outflow filter (also a wall for a particle) boundary, a particle reflection routine was implemented such that the particle was repositioned inside the domain.

The reflection conditions that mimic particle-wall collisions are implemented in BRUSH as follows. A particle is repositioned inside the domain when it hits a solid boundary wall using two different reflection mechanisms, i.e., perfect reflection and random reflection, biased towards the inside of the domain. Both mechanisms model elastic wall collisions, i.e., no kinetic energy is absorbed in the collision. It should be noted that in practice elastic collisions, particle-wall and particle-particle, lead to a loss of energy, e.g., see Russell et al. (2014); Boettcher et al. (2017). This phenomenon is not included in our model. Perfect reflection is performed when the start point $\boldsymbol{x}_{\text{old}}$ of the particle movement is well inside the domain (distance from the hull intersection point is greater than some positive value ε). Then, the new position $\tilde{\boldsymbol{x}}_{\text{end}}$ of the particle is computed in a two stage process. The reflection direction $\mathbf{e}$ is

$$\mathbf{e} = (\boldsymbol{x}_{\text{hull}} - \boldsymbol{x}_{\text{old}}) - 2\left((\boldsymbol{x}_{\text{hull}} - \boldsymbol{x}_{\text{old}}) \cdot \mathbf{n}\right)\mathbf{n},$$

where $\mathbf{n}$ is the outward pointing unit normal of that tetrahedra face where $\boldsymbol{x}_{\text{hull}}$ is located, and the norm of the reflection vector is set to be

$$\|\tilde{\boldsymbol{x}}_{\text{new}} - \boldsymbol{x}_{\text{hull}}\| = \|\boldsymbol{x}_{\text{new}} - \boldsymbol{x}_{\text{hull}}\|.$$

Random reflection is performed whenever either the starting point of a reflection is very close to the wall, or in case a double reflection would occur. Both cases are very prone to robustness errors, therefore we decided to handle them in this more stable manner. Random reflection is performed with an acceptance-rejection scheme. Directions $\mathbf{e}$ on the "inward" half sphere of radius $r := \|\boldsymbol{x}_{\text{new}} - \boldsymbol{x}_{\text{hull}}\|$ are created by drawing two random numbers $u_1, u_2 \sim \mathscr{U}[0,1]$ and setting

$$\mathbf{e} = r\left(\sqrt{1-z^2}\cos(\theta), \sqrt{1-z^2}\sin(\theta), z\right), \quad \theta = 2\pi u_1, \quad z = -1 + 2u_2.$$

If the scalar product $\mathbf{e} \cdot \mathbf{n}$ is positive, the direction $\mathbf{e}$ is inverted, in order to point inwards. Further, a check is performed whether $\boldsymbol{x}_{\text{hull}} + \mathbf{e}$ is inside the domain. If so, that value is accepted and the particle moved there, otherwise $\mathbf{e}$ is rejected and another random reflection direction is generated.

In fact, there are more cases of non-robustness, and several of them are just handled by relocating particles to cell centers. In each simulation, the occurrence of such cases is counted, and it turned out that around one in every 10^7 reflections fell into that category. Therefore, this issue is negligible for the overall results. The particle reflection algorithm is illustrated in Figure 6 and more details can be found in Bartsch (2018).

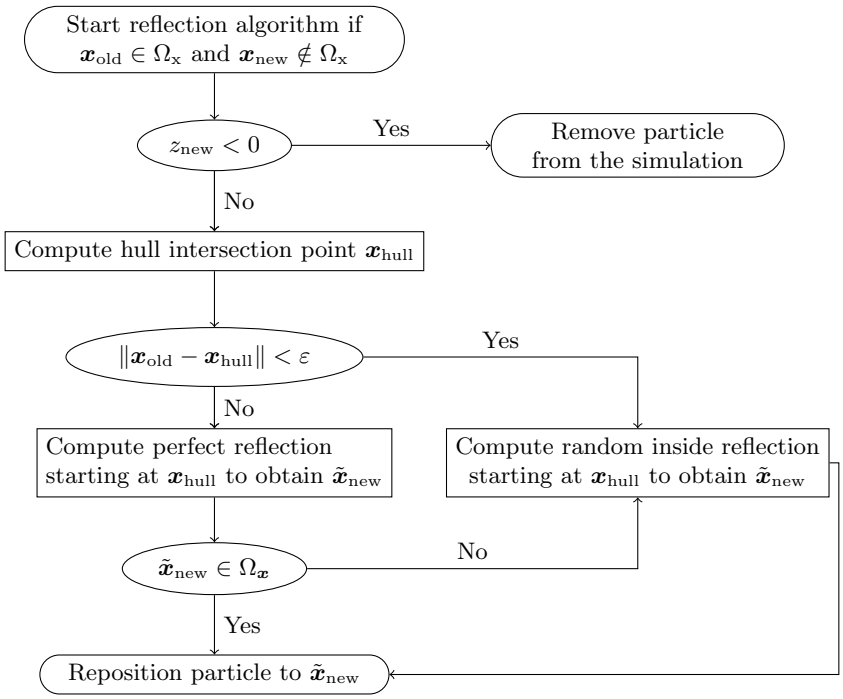

Figure 6: The particle reflection algorithm that was implemented in BRUSH. The former position of the particle is $\boldsymbol{x}_{\text{old}}$, the new (outside) position is $\boldsymbol{x}_{\text{new}}$, with z-component z_{new}. A small $\varepsilon > 0$ is given as wall vicinity tolerance.

4.3. Sedimentation

One of the desired effects of the FBC is a height separation of different crystal size fractions. To reflect such a behavior in simulations, sedimentation has to be taken into account. For the simulations presented in Section 5, a sedimentation model for spherical particles was implemented in BRUSH, whose derivation and formulation can be found in Berg (1983, pp. 58). Since in the actual experiments, the particles deviate from a spherical form, we found it necessary to modify this model for our purposes.

Sedimentation of particles is modeled via a sedimentation rate, which results in a downward sinking velocity of particles and differs for different particle sizes. In order to apply the sedimentation rate that was proposed by Berg (1983), two assumptions must be made: the particles are spherical and the fluid velocity around the particles is so low that Stokes' law is a sufficiently good approximation for the inverse particle mobility (frictional drag coefficient). Its derivation starts from a formula for the sinking velocity $\boldsymbol{u}_s$ of a particle which

is surrounded by moving fluid molecules:

$$\boldsymbol{u}_s = \frac{\mathbf{F}_{\text{down}}}{f_d}. \tag{7}$$

Here, $\mathbf{F}_{\text{down}}$ [N] is the force acting downwards and f_d [$^{\text{kg}}/_{\text{s}}$] is the frictional drag coefficient, which relates force and velocity. The frictional drag coefficient is related to the particle mobility μ_{ES} of the Einstein–Smoluchowski relation by $\mu_{ES} = 1/f_d$. Specifying the forces acting downwards in (7), those are $\|\mathbf{F}_{\text{down}}\| = (m - V\rho)g$. In this equation, m is the particle mass, V the particle volume, ρ is the density of the displaced fluid, and the gravity $g = 9.81$ $^{\text{m}}/_{\text{s}^2}$. The force depends linearly on the mass difference of particle and displaced fluid. Other forces that might occur in swirling flows, so-called dynamic pressure gradient forces, are neglected by expecting that the hydrostatic pressure gradient dominates. It remains to find a model for f_d. Here is where Stokes' law for spherical particles in a viscous fluid at low velocity comes into play, and thus the two assumptions made above. According to that model, see Berg (1983, pp. 58) for its detailed derivation, f_d can be approximated as $f_d = 3\pi\mu d$, with d being the diameter of the spherical particle, and μ the dynamic fluid viscosity.

Applying the sedimentation model derived in this way in our simulations, we encountered severe difficulties. The larger particles entering through the inlet with slower velocities were unable to counteract the gravitational force. Depending on the boundary conditions (particle removal/reflection) at and around the inlet, the model could result with excessive agglomeration or significant loss of particles. The two assumptions from above are satisfied probably only to some extent. To mitigate these difficulties, we decided to modify the sedimentation model from the literature by introducing a scaling factor $\sigma \in [0, 1]$. Then, inserting everything in (7) and replacing $m = V\rho_{\text{cryst}}$, one finally obtains the following equation for the additional, downwards directed velocity component:

$$u_z = \sigma d^2 \cdot \frac{(\rho_{\text{cryst}} - \rho)g}{18\mu}, \quad \sigma \in [0, 1],$$

or equivalently in the mass-based formulation:

$$u_z = \sigma \frac{\left(\frac{6}{\rho\pi}\right)^{\frac{2}{3}} (\rho_{\text{cryst}} - \rho)g}{18\mu} m^{\frac{2}{3}}, \quad \sigma \in [0, 1]. \tag{8}$$

An appropriate value for σ was found by numerical simulations, see Section 5.2.

5. Computational Results and Their Validation Against Experiments

The crystallization device, described in Section 2, is virtually configured and discretized. In this section, results of the numerical simulation using the models

and algorithms, as described in Section 3 and 4, will be discussed. The simulation time is $t_{end} = 1800$ s $= 30$ min. The macroscopic values of density and viscosity are kept constant during the course of the simulations since the temperature varies only slightly (± 1 K), and the crystal load is almost negligible. The flow field is developed in the first 30 s and the particles are inserted thereafter in the interval $[30\text{ s}, 40\text{ s}]$. In the experiments, the particles are funneled into the device all at once, however, in the simulations, the particles enter the domain over a short time interval, since the SPS works better with a relatively uniform spatial distribution of particles.

For the initial investigation of numerical parameters, the seed mass of 1×10^{-4} kg is divided equally between two fractions of particles, one for particles of diameter 75 μm and one for particles of diameter 125 μm. The fractions are represented by either a monodisperse or a log-normal distribution with 25 μm standard deviation. The model is described in terms of particle mass, however, for better understanding of computational results and its comparison against experiments, the particle sphere equivalent diameter in μm is used.

A typical run took around 35 hours computing time on a single core, where the majority of the time (around 75 %) was spent for the flow simulation.

5.1. Flow Field Simulations

For the simulations, the mass flow rates of $\dot{m} = 56$ kg/h and $\dot{m} = 93$ kg/h are considered. The filter width δ of the Smagorinsky LES model, see Table 2, was chosen to be $2h_K$, where h_K is the shortest edge of the tetrahedron K. Parameter studies showed that the value $C_{\text{Smago}} = 5 \cdot 10^{-4}$ for the Smagorinsky coefficient is appropriate. With this value, the LES model does not add too much artificial viscosity. Simulations of the velocity field were performed on grids with different levels of refinement. All of them gave the same principal flow pattern, see Bartsch (2018) for details. Instantaneous cross-sectional flow fields for mass flow rates of 56 kg/h and 93 kg/h are illustrated in Figure 7. The principal form of the flow field, with the dominating jet in the center, is the same for the whole time interval. Due to the dominating jet, the evolution of the flow structures away from the center is hard to visualize.

Fluidized beds are applied when impellers and breakage shall be avoided, since the fluid velocities and turbulence intensity are low. Stirred crystallizers lead to better mixing and even stronger mixing in small regions can be achieved by jet crystallizers. Figure 7 shows a jet like behavior at the inlet of the device. The remaining part of the crystallizer is characterized by small velocity magnitudes and it therefore resembles a fluidized bed in these areas.

We performed flow simulations also on finer grids than used for the population balance system (1a)–(1d), see (Bartsch, 2018, Chapter 7.2). These finer grids were obtained by refining the grid presented in Figure 5 once or twice. While

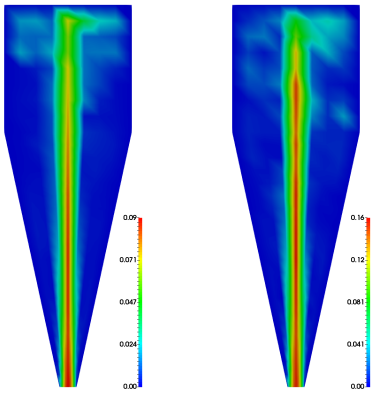

Figure 7: Instantaneous flow field (norm of the velocity in $^{\mathrm{m}}/_{\mathrm{s}}$) in a vertical cut plane after 200 s; left: inflow 56 $^{\mathrm{kg}}/_{\mathrm{h}}$, right: inflow 93 $^{\mathrm{kg}}/_{\mathrm{h}}$.

more details of the flow field could be resolved on the finer grids, the main features of the flow, i.e., the central jet and the vortices near the filter, could be observed on all grids. Since the library for the stochastic particle simulation is not yet parallelized, we had to perform the simulations for the population balance system in a sequential way. Thus, for the reason of computing time, we could not afford to perform simulations of the population balance system on the finer grids, see above for information on the computing time on the grid from Figure 5.

5.2. Coupled Simulation of Temperature, Concentration, and Population Balance of Potash Alum Crystals

Here, we will present results for the coupled simulations. The parameters for each of the equations are also described.

For the temperature field computations using equation (1b), we use $D_T = 1.5 \cdot 10^{-7}$ $^{\mathrm{m}^2}/_{\mathrm{s}}$ and $g_T = 0.0221$ $^{\mathrm{K}\cdot\mathrm{m}^3}/_{\mathrm{kg}}$, utilizing the function expression and constants in Table 2. The Dirichlet boundary values for the temperature over time are linearly interpolated over the initial temperature at $t = 0$ min, i.e., $T_{\mathrm{start}} = 288.95$ K (15.8°C), and the temperature at the end of the experiment after $t = 30$ min, i.e., $T_{\mathrm{end}} = 288.35$ K (15.2°C).

The diffusion constant D_c in the concentration equation (1c) is given in Table 2 and for M_{hydrate} the value for potash alum is taken, see also Table 2. In the simulations, the initial condition $c_{\mathrm{start}} = 207$ $^{\mathrm{mol}}/_{\mathrm{m}^3}$ was chosen. This value corresponds to the saturation concentration at 17 °C.

Storage for a maximum of 256 computational particles was assigned to each mesh cell of $\Omega_{\boldsymbol{x}}$. The conversion from computational particle count in the SPS

to physical particle concentration is linearly proportional to the physical particle concentration which a full ensemble represents. In preliminary simulations, 5.0×10^8 # physical particles/m^3 was found to be an appropriate upper bound for the physical particle concentration in the majority of the systems and the conversion factor chosen so that this corresponded to a full ensemble of 256 computational particles. This conversion factor was used throughout the domain except close to the bottom of the device where physical particle concentration was higher due to sedimentation. To numerically capture these higher concentrations the conversion factor was increased by a factor of 10 below 0.1 m and by a factor of 100 below 0.05 m. The choice of conversion factor is a purely numerical matter, it influences computational cost and numerical precision, but apart from this has no effect on the results for physical quantities. This setup led to a total of roughly 150000 computational particles in the simulation domain after completion of the insertion at 40 s. That number is typically reduced by around 50% at the end of a simulation, see Bartsch et al. (2019); Patterson et al. (2011) for a detailed discussion of the simulation steps and how they affect the computational particle count.

Determining an Appropriate Sedimentation Coefficient

Numerical results, shown in Figure 8, suggested that the sedimentation was overly dominant using $\sigma \geq 0.5$ in the sedimentation model (8). In some test simulations, up to 80 % of the total crystal mass was lost over time that way. In the actual experiment, the octahedral shape and agglomerate nature of the potash alum crystals led to a greater particle surface and porosity, which suggests that the actual sedimentation velocity was less than for spherical particles. The sedimentation of particles could be effectively downscaled using $\sigma < 0.5$. From the numerical results shown in Figure 8, one can conclude that $\sigma = 0.1$ is an appropriate choice.

For this sedimentation coefficient, according to Equation (8), the sedimentation velocity for a particle of 100 μm diameter becomes -0.0003 m/s. At the outlet at the top of the crystallizer and near the vessel walls, the fluid velocity approaches zero as well. Hence, the relative particle velocity is small. The particle does not leave the vessel at the top. Instead, it sinks down near the vessel walls.

Determining an Appropriate Agglomeration Parameter

With the sedimentation parameter fixed to $\sigma = 0.1$, simulations with different agglomeration parameters were performed, comparing the development of the PSD. The main goal was to examine the dependence of the PSD on the height in the device, where the particle sampling was performed. Simulation data was gained by saving snapshots of all computational particles present in the simulation domain every 10 seconds. This interval was large enough to ensure

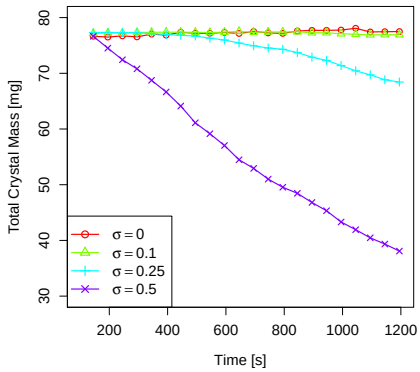

Figure 8: Total crystal mass in the system during agglomeration-only simulations with different sedimentation parameters σ. Significant mass loss occurs for $\sigma = 0.5$. For $\sigma = 0.1$, there is almost no mass loss. Start mass was 77 mg, mass flow rate 56 $^{\mathrm{kg}}/_{\mathrm{h}}$, agglomeration parameter $\kappa = 500$.

a complete exchange of particles in each ensemble, thus reducing stochastic dependence, and allowing for averaging over multiple of these snapshots without too much redundancy. This way, between 2 and 3 GB of data were collected per simulation. Additionally, all particles that left the device through the inflow were logged.

Figures 9 and 10 show spatially summed, resp. averaged, quantities. In Figure 9, the development of the total particle mass is shown for both flow setups. A gain due to growth is visible, followed at later times by mass loss through the inlet. The latter is the more pronounced for larger agglomeration parameters, since larger particles sediment faster and carry more mass out of the domain upon exit. Note also that mass gain due to particle growth is higher in the slower flowing setup. From Figure 10, one observes that the difference in the development of the spatial average particle diameter is less distinct between the two flow setups. The average increase in particle size in the setup with low flow rate of 53 $^{\mathrm{kg}}/_{\mathrm{h}}$ is only slightly larger than in the setup with higher flow rate of 93 $^{\mathrm{kg}}/_{\mathrm{h}}$. The flow rate affects the supersaturation and, hence, the growth and agglomeration rate only to a small extent. As was expected, a higher agglomeration parameter results in larger particles in total.

From the comparisons with experimental results, we concluded that $\kappa = 5000$ is an appropriate parameter. This parameter is of the same order of magnitude as in Anker et al. (2015).

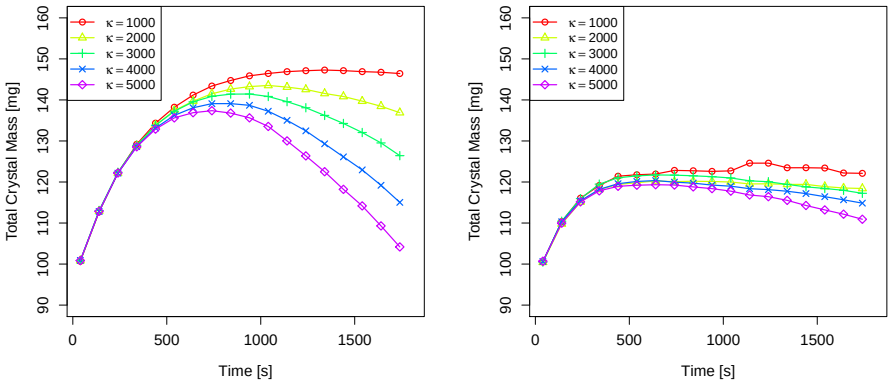

Figure 9: Development of the total crystal mass, depending on agglomeration scaling parameter κ. Higher agglomeration rates result in larger particles, which are more likely to slip out through the inlet due to sedimentation. Left: 56 $^{\mathrm{kg}}/_{\mathrm{h}}$ mass flow setup. Right: 93 $^{\mathrm{kg}}/_{\mathrm{h}}$ mass flow setup.

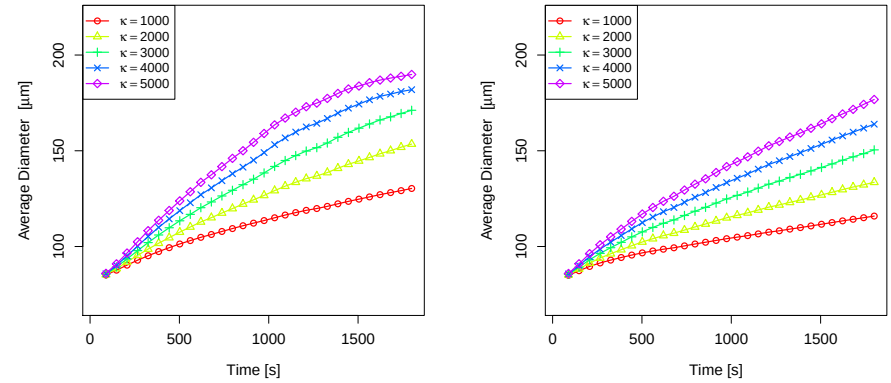

Figure 10: Temporal development of the spatially averaged particle diameter in the crystallizer device, depending on agglomeration scaling parameter κ. Left: 56 $^{\mathrm{kg}}/_{\mathrm{h}}$ mass flow setup. Right: 93 $^{\mathrm{kg}}/_{\mathrm{h}}$ mass flow setup.

5.3. Simulations versus Experiments

In the experiments, 1×10^{-4} kg of crystalline seeds were used and their experimentally measured distribution is shown in Figure 11.

For the simulations, the distribution was approximated as two lognormal distributions with the help of `fitdistrplus` package in R language, see Delignette-Muller and Dutang (2015). A call to the `fitdist` function with the arguments

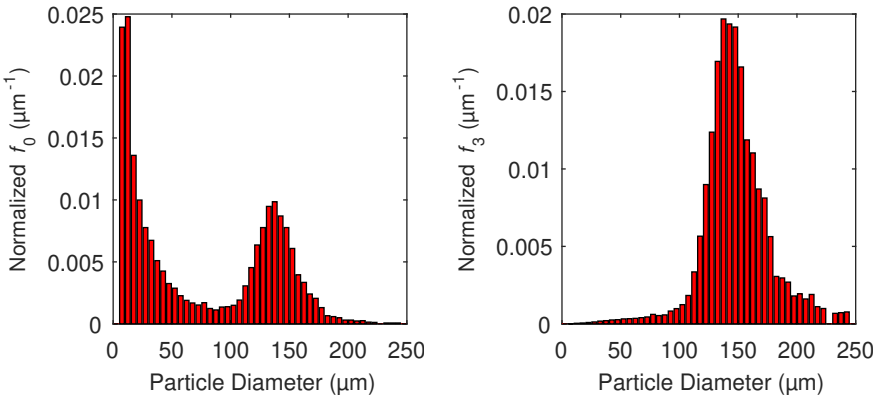

Figure 11: Initial crystal size distribution in the first 60 s of experiment C. Distributions are normed by their sum and the size class width. Left: Number density distribution; Right: Mass density distribution.

	Main particle fraction	Dust particle fraction
$\bar{m}_{\mathrm{diam}}$ in μm	129.2	9.5
$\mathrm{sd}_{\mathrm{diam}}$ in μm	26.2	7.9
μ_{diam}	4.8	2.0
σ_{diam}	0.2	0.7
μ_{N}	35.4	26.8
σ_{N}	0.6	2.2

Table 3: Data of the artificial initial distribution, a sum of the two lognormal distributions 'main' and 'dust'. Mean value $\bar{m}_{\mathrm{diam}}$ and standard deviation $\mathrm{sd}_{\mathrm{diam}}$ of the diameter, parameters of the lognormal distributions in terms of the diameter (μ_{diam}, σ_{diam}) and in terms of number of potash alum molecules (μ_{N}, σ_{N}).

'lnorm' and 'mme' evoked a moment matching estimation algorithm, which returned parameters of a lognormal distribution which had the same first and second moments as the input data. Those parameters are listed in Table 3, along with their equivalents in terms of numbers of molecules, which were used as input data for the simulations.

Figure 12 shows the development of the particle size over time at various sample heights (z-coordinate) in the crystallizer for the simulations and experiments. In Figure 12 (left), the value at coordinate z comprises all computational particles in the interval $[z - 0.025, z + 0.025]$ of 5 cm width. The computational results show that the difference in average particle size is the most distinct at the bottom of the crystallizer. There is hardly a difference between the curves for heights greater than 0.17 m. This could be explained by the fact that the particles have a longer residence time in the vicinity of the filter, where they get reflected repeatedly and travel slowly to the sides of the device. This large residence time could lead to more agglomerations taking place in those cells close to

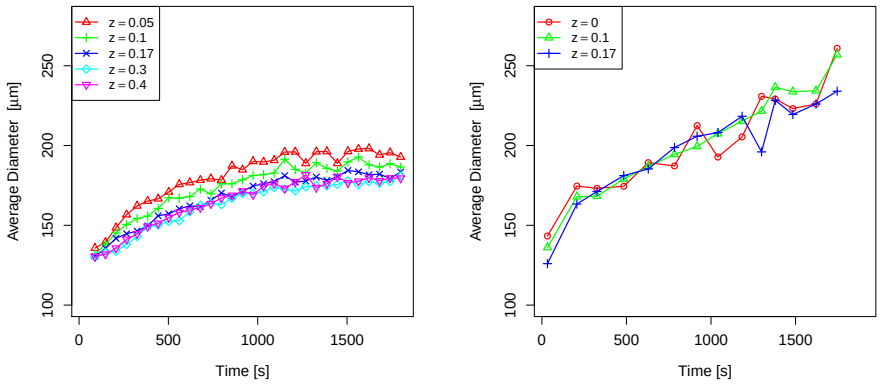

Figure 12: Temporal development of the (averaged) crystal diameter in different heights in the crystallizer device for 56 $^{\mathrm{kg}}/_{\mathrm{h}}$ mass flow setup. The height z is given in m above the inlet. Left: Simulation results with agglomeration parameter $\kappa = 5000$ and sedimentation parameter $\sigma = 0.1$. Right: Experimental observations.

the top boundary. Finally, it can be observed that the experimental and computational results are qualitatively the same: there is a consistent increase in the particle size at all heights over time. Quantitatively there are some differences. In the experiments, the relationship between average diameter and time is approximately linear while it seems to be sub linear in the simulations. Although, the average diameter is within the same range for all heights, it increased by about 60 μm in the simulations and around 80 μm in the experiments. The observed difference in Figure 12 may be related to experimental and modeling issues, see a discussion of the latter ones towards the end of this section. Concerning the experiments, one issue might be the sampling of crystals within the measurement loop. Crystals are withdrawn for the optical observation at a specific height but also due to technical limitations at a specific distance from the center of the FBC. For the simulation results, we count and evaluate all particles in the same height range from center to the vessel wall. As this will include more and therefore also more smaller crystals, the average crystal size may be smaller in comparison to the experiments. At the same time, a larger size separation by the crystallizer height was observed in the simulations but not in the experiments. The specific withdrawal point in our experiment can also influence the size separation effect. The observed difference between experimental and simulated data calls for more detailed analysis in the future. Whether this effect is helpful for a selective product removal is an interesting and open question when implementing the FBC in a real application.

Figure 13 shows the PSD for different heights at 15 and 30 min for the simulations and experiments. The sample heights were chosen in accordance with Figure 12. In Figure 13 (left), the computational particles were organized in

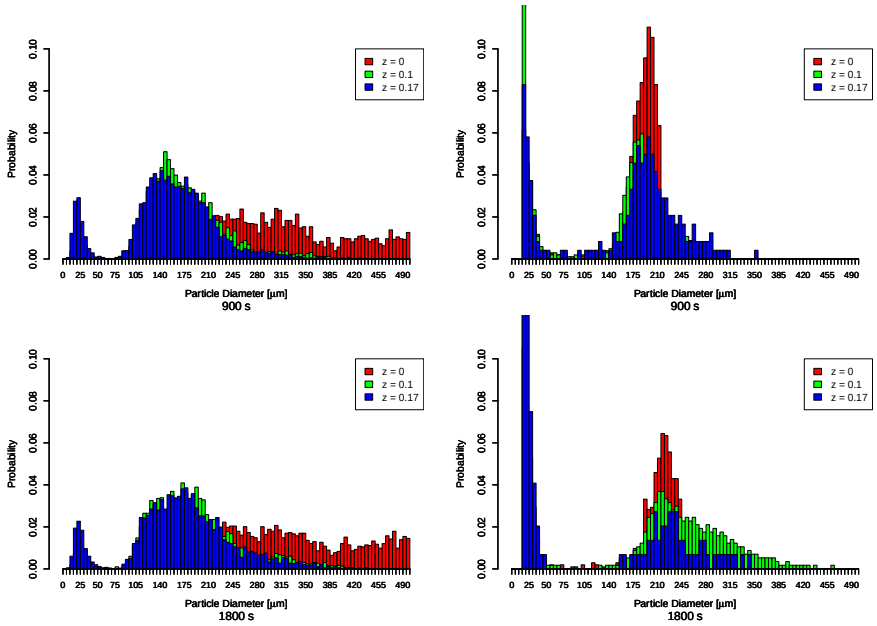

Figure 13: Snapshots of the PSD at different points in time and in different heights in the crystallizer. All figures were obtained with agglomeration parameter $\kappa = 5000$ and sedimentation parameter $\sigma = 0.1$. The initial distribution is the sum of two log-normal distributions. Left: Simulations. Right: Experiments.

bins according to their diameter, where the height of the bar is the probability of a random physical particle to fall into the bin. The histograms represent particle populations at the given particular point in time. A perceptible shift in the PSD is observed. In Figure 13 (left), it can be seen that a relatively widespread population of large particle agglomerates are formed near the inlet. At heights 0.1 m and 0.17 m, smaller particles were present that had experienced possibly less collision and surface growth events. Comparing the distributions with the initial distribution in Figure 11, the height of the peak reduces, the distribution widens and it moves to larger sizes for all heights, for both experiments and simulations. The initial peak is at 130 μm and after 30 min the peak is at about 190 μm and 210 μm for the simulations and experiments, respectively. This suggests a considerable increase in crystal size.

A reason for the increase in the distribution width and the tailing towards larger sizes is certainly agglomeration. In the experiments, the degree of agglomeration stayed constant or increased only slightly, which does not mean that agglomeration cannot occur. The event of an agglomerate agglomerating again reduces the degree of agglomeration in terms of number which could be equalized by the agglomeration of primary crystals. This assumption is supported by a slight decrease in the total crystal number in the intermediate position in Figure 3.

Since the total crystal number decreases during the process, breakage seems to be unlikely. Breakage and agglomeration may be in equilibrium and would then not have an observable effect in the experiments. This is also improbable since there are no new crystals appearing in Figure 13 at the lower end of the seed size range during the experiments. Hence, it seems to be justified that breakage can be neglected in our model.

In our opinion, the main reason for the quantitative differences of experimental and numerical results is the modeling of the particles by just one internal coordinate (mass). As already mentioned, the potash alum crystals are of octahedral shape. Thus, given the mass of a particle, it is not possible to fully determine its shape and size. The stochastic particle simulation method is a natural framework for modeling particles in a more complex way than with one internal coordinate (Sander et al., 2011; Shekar et al., 2012). Developing a particle model that is more realistic in this respect will be a topic of future research and should be combined with a consideration of the interaction of the particles with the unresolved flow scales. Further modeling aspects whose improvement should be studied in future are the agglomeration kernel and the sedimentation model. Future work includes also the MPI parallelization of the library for the SPS. Then, since the code for the CFD is already MPI parallelized, it will be possible to perform simulations of the population balance system on much finer grids in affordable times on clusters with many processors. Besides the general expectation of computing more accurate results on finer grids, in particular more flow scales can be resolved.

Because of the differences of experimental and numerical results, we also took into consideration whether the withdrawal flow in the experiments may have influenced the flow, induced turbulence, and disturbed the size separation. Additional simulations at the higher mass flow rate of 93 $^{\mathrm{kg}}/_{\mathrm{h}}$ contradict this idea since the resulting distributions look similar to the distributions in Figure 13. One might tend to think that the withdrawal to the sampling loop is not isokinetic. The size distribution of the crystals in the first or second minute after seed addition are slightly smaller for the bottom seeding method, where the seeds enter the system through the cuvette, compared to top seeding, where the crystals are sampled at the withdrawal tube. Hence, the withdrawal might slightly overselect large crystals. The difference between the seeding methods is only in the range of a few μm. Hence, the withdrawal is nearly isokinetic and the explanation can be invalidated.

6. Summary and Outlook

This paper presented an investigation of a crystallization process in an FBC, both by experiments as well as by numerical simulations based on a population balance model. A stochastic-deterministic method with novel extensions was

used for performing the simulations. Comparisons of experimental and numerical results showed a good qualitative and a reasonable quantitative agreement. Possible reasons for the quantitative differences were discussed in Section 5.3.

We think that future experiments could focus on a better fluidization of the crystals for fractionation. This might be reached either by decreasing the seed crystal size, by increasing the inflow velocity, by changing the crystallizer geometry, or by modifying the crystallizer inlet. In the experiments, the absolute number of crystals at a height of 0.17 m and 0.30 m becomes negligible. A separation in height by crystal size might be difficult close to the inlet. In this respect, we think that an increased flow rate in the main circuit may increase the fluidization of the crystals. In the simulations, an upward fluid flow was mainly observed at the axis of the FBC. In the work of Kerst et al. (2017), a slim FBC was considered and higher vertical particle velocities with lower distance from the vertical crystallizer axis were measured. Their fluid velocities were qualitatively similar to those in the present paper.

Among the several ways that were used to simplify the model, the modeling of the potash alum crystals with just one property coordinate was considered to be one of the main reasons for the quantitative differences of the results. The stochastic particle simulation method provides a natural framework for the simulation of particles that are modeled in a more complex way than with one property. Thus, the implementation of a multi-property particle model for the crystallizer is one of the most important next steps for the simulations.

Acknowledgment

The work of V. John and K. Sundmacher was supported by grants Jo329/10-3 and SU189/6-3 within the DFG priority programme 1679: Dynamic simulation of interconnected solid processes. R. Patterson has been partially supported by the Deutsche Forschungsgemeinschaft (DFG) through grant CRC 1114 "Scaling Cascades in Complex Systems", Project C08. We would also like to acknowledge the support of Hang Si for assisting in the mesh generation using TetGen.

References

Ahmed, N., Bartsch, C., John, V., Wilbrandt, U., 2018. An assessment of some solvers for saddle point problems emerging from the incompressible Navier–Stokes equations. Comp. Meth. Appl. Mech. Eng. 331, 492–513.

Anker, F., Ganesan, S., John, V., Schmeyer, E., 2015. A comparative study of a direct discretization and an operator-splitting solver for population balance systems. Comput. Chem. Eng. 75, 95–104.

Bartsch, C., 2018. A coupled stochastic-deterministic method for the numerical solution of population balance systems. Ph.D. thesis, Freie Universität Berlin, Department of Mathematics and Computer Science.

Bartsch, C., John, V., Patterson, R. I., 2019. Simulations of an asa flow crystallizer with a coupled stochastic-deterministic approach. Computers & Chemical Engineering 124, 350 – 363.

Beckmann, W. (Ed.), 2013. Crystallization : basic concepts and industrial applications. Wiley-VCH, Weinheim.

Berg, H. C., 1983. Random walks in biology. Princeton University Press, Princeton, NJ.

Binev, D., 2015. Continuous fluidized bed crystallization. Ph.D. thesis, Otto-von-Guericke-University Magdeburg, Faculty of Process and Systems Engineering.

Boettcher, R., Russell, A., Mueller, P., 2017. Energy dissipation during impacts of spheres on plates: Investigation of developing elastic flexural waves. International Journal of Solids and Structures 106-107, 229 – 239.

Borchert, C., Temmel, E., Eisenschmidt, H., Lorenz, H., Seidel-Morgenstern, A., Sundmacher, K., 2014. Image-based in situ identification of face specific crystal growth rates from crystal populations. Cryst. Growth Des. 14 (3), 952–971.

Celnik, M., Patterson, R. I. A., Kraft, M., Wagner, W., 2007. Coupling a stochastic soot population balance to gas-phase chemistry using operator splitting. Combust. Flame 41 (2), 158–176.

Davis, T. A., 2004. Algorithm 832: UMFPACK V4.3—an unsymmetric-pattern multifrontal method. ACM Trans. Math. Software 30 (2), 196–199.

Delignette-Muller, M. L., Dutang, C., 2015. fitdistrplus: An R package for fitting distributions. J. Stat. Softw. 64 (4), 1–34.

Ganesan, S., John, V., Matthies, G., Meesala, R., Abdus, S., Wilbrandt, U., 2016. An object oriented parallel finite element scheme for computing pdes: Design and implementation. In: IEEE 23rd International Conference on High Performance Computing Workshops (HiPCW) Hyderabad. IEEE, pp. 106–115.

Garcia-Gutierrez, L., Hernández-Jiménez, F., Cano-Pleite, E., Soria-Verdugo, A., 2017. Improvement of the simulation of fuel particles motion in a fluidized bed by considering wall friction. Chem. Eng. J. 321, 175–183.

Hoffmann, A., Janssen, L., Prins, J., 1993. Particle segregation in fluidised binary mixtures. Chem. Eng. Sci. 48 (9), 1583–1592.

Howley, M. A., Glasser, B. J., 2002. Hydrodynamics of a uniform liquid-fluidized bed containing a binary mixture of particles. Chem. Eng. Sci. 57 (19), 4209–4226.

John, V., 2016. Finite element methods for incompressible flow problems. Vol. 51 of Springer Series in Computational Mathematics. Springer, Cham.

John, V., Novo, J., 2012. On (essentially) non-oscillatory discretizations of evolutionary convection-diffusion equations. J. Comput. Phys. 231 (4), 1570–1586.

John, V., Schmeyer, E., 2008. Finite element methods for time-dependent convection-diffusion-reaction equations with small diffusion. Comput. Methods Appl. Mech. Engrg. 198 (3-4), 475–494.

Kerst, K., Roloff, C., de Souza, L. G. M., Bartz, A., Seidel-Morgenstern, A., Thévenin, D., Janiga, G., 2017. CFD-DEM simulations of a fluidized bed crystallizer. Chem. Eng. Sci. 165, 1–13.

Kuzmin, D., 2009. Explicit and implicit FEM-FCT algorithms with flux linearization. J. Comput. Phys. 228 (7), 2517–2534.

Lewis, A. E., Seckler, M. M., Kramer, H. J., Rosmalen, G. v., 2015. Industrial crystallization : fundamentals and applications. Cambridge Univ. Press, Cambridge.

Lin, W., Dam-Johansen, K., Frandsen, F., 2003. Agglomeration in bio-fuel fired fluidized bed combustors. Chem. Eng. J. 96 (1), 171–185, festschrift Prof. Cor M. van den Bleek.

Nienow, A. W., Naimer, N. S., 1980. Continuous mixing of two-particulate species of different density in a gas fluidised bed. Trans. IChemE 58, 181–186.

Park, G. I., Bassenne, M., Urzay, J., Moin, P., Apr 2017. A simple dynamic subgrid-scale model for les of particle-laden turbulence. Phys. Rev. Fluids 2, 044301.

Patterson, R. I., Wagner, W., Kraft, M., 2011. Stochastic weighted particle methods for population balance equations. J. Comput. Phys. 230 (19), 7456–7472.

Russell, A., Müller, P., Shi, H., Tomas, J., 2014. Influences of loading rate and preloading on the mechanical properties of dry elasto-plastic granules under compression. AIChE Journal 60 (12), 4037–4050.

Saad, Y., 1993. A flexible inner-outer preconditioned GMRES algorithm. SIAM J. Sci. Comput. 14 (2), 461–469.

Sander, M., Patterson, R. I. A., Braumann, A., Raj, A., Kraft, M., 2011. Developing the PAH-PP soot particle model using process informatics and uncertainty propagation. Proc. Combust. Inst. 33, 675–683.

Seckler, M., Bruinsma, O., Rosmalen, G. V., 1996. Phosphate removal in a fluidized bed—i. identification of physical processes. Water Res. 30 (7), 1585–1588.

Shekar, S., Smith, A. J., Menz, W., Sander, M., Kraft, M., 2012. A multidimensional population balance model to describe the aerosol synthesis of silica nanoparticles. J. Aerosol Sci. 44, 83–98.

Si, H., 2015. TetGen, a Delaunay-based quality tetrahedral mesh generator. ACM Trans. Math. Software 41 (2), Art. 11, 36.

Smagorinsky, J., 1963. General circulation experiments with the primitive equations. Mon. Wea. Rev. 91, 99–164.

Tavare, N. S., 1995. Industrial crystallization : process simulation analysis and design. The Plenum chemical engineering series. Plenum Press, New York, NY.

Temmel, E., Eisenschmidt, H., Lorenz, H., Sundmacher, K., Seidel-Morgenstern, A., 2016. A short-cut method for the quantification of crystallization kinetics. 1. Method development. Cryst. Growth Des. 16 (12), 6743–6755.

Wilbrandt, U., Bartsch, C., Ahmed, N., Alia, N., Anker, F., Blank, L., Caiazzo, A., Ganesan, S., Giere, S., Matthies, G., Meesala, R., Shamim, A., Venkatesan, J., John, V., 2017. ParMooN—A modernized program package based on mapped finite elements. Comput. Math. Appl.

Zhang, Y., Jin, B., Zhong, W., Ren, B., Xiao, R., 2009. Characterization of fluidization and segregation of biomass particles by combining image processing and pressure fluctuations analysis. Int. J. Chem. React. Eng. 7 (1), A81.